Capillarity Effects on Crystallization Kinetics: Insulin

Ilya Reviakine, Dimitra K. Georgiou, and Peter G. Vekilov*

Contribution from the Department of Chemical Engineering, University of Houston, Houston, Texas 77204-4004

Received March 26, 2003; E-mail: vekilov@uh.edu

Abstract: During layerwise growth of crystals, capillarity governs the generation of new crystal layers. Theory predicts that the line tension of the layer edge determines, via the characteristic two-dimensional capillary length L_c, the rates of generation and initial growth of the new layers. To test the correlation between L_c and the rate of layer generation, we used in situ Tapping Mode Atomic Force Microscopy (TM-AFM) to study the generation and spreading of layers during crystallization of rhombohedral, R3, porcine insulin. We show that crystallization of this insulin form is uniquely suitable for such an investigation due to the linear kinetics of step growth it exhibits. This linear kinetics reflects the abundance of the incorporation sites along the rough steps, the lack of long-range step−step interactions, and the transport control of the growth kinetics. The kinetic coefficients are 7×10^{-3} and 4×10^{-2} cm s^{-1}, respectively, in the absence and presence of the cosolvent acetone—somewhat high for proteins and comparable to values for inorganic systems. We show that (i) the relevant capillary length, the size of a critical quadrangular 2D nucleus L_c, is the main scaling factor for the density of growth steps, while (ii) all steps longer than L_c grow with a rate determined only by the supersaturation and independent of their length. We explain the divergence of (ii) from theoretical predictions with the high supersaturations typical of the growth of this protein system.

Introduction

Crystals, whose interfaces with their medium are characterized by high surface free energy, are smooth on the lengthscale of their building blocks: atoms, molecules, or particles.[1] Such crystals are faceted by planes with low Miller indices[2] and grow by the generation and spreading of new layers, with the building blocks attaching to the edges of the unfinished layers, the steps.[3,4] This growth mode is several orders of magnitude slower than the growth of crystals with rough surfaces.[5] The thermodynamic effects on the kinetics of layerwise crystallization do not end with the selection of the growth mode. Capillarity, via the line tension of the edge of the emerging layers, determines the rate of generation of new layers either by two-dimensional nucleation[4,6] or by screw dislocations piercing the growing face.[7]

In this paper, we examine the role of capillarity in the generation of new steps by screw dislocations. Since one of the step's ends is pinned at the dislocation outcrop and the step's velocity is preserved along its length, the step winds in a spiral around the dislocation.[7] The thermodynamic principles which form the foundation of the theories of dislocation growth of crystals are as follows: (i) steps shorter than a critical length, or, in the case of curved steps, with curvature greater than a

critical value, do not grow; (ii) steps with lengths (or curvatures) comparable to this critical value grow at reduced rates; (iii) the combination of factors (i) and (ii) determines the frequency of rotation of the spiral and the growth rate of the crystal. Statements (i) and (ii) are manifestations of the two-dimensional Gibbs−Thomson (Kelvin) effect, which states that phases of sizes comparable to a characteristic capillary length L_c have an increased chemical potential. As a consequence, those smaller than L_c dissolve even in supersaturated media,[8,9] while the growth of those only slightly larger than L_c is driven by a diminished force.[9]

Experimental tests of the above principles require a system with the following properties: (i) noninteracting steps, so that minor variations in step density do not affect the step velocity;[10] (ii) lack of step bunching, which would skew the determination of the density of the steps;[11,12] (iii) linear kinetics of step propagation, so that the capillarity reduction of the driving force could be directly observed through its effect on the step velocity. A previous study of the thermodynamics of calcite crystallization found strong modifications of the effects of capillarity due to the paucity of incorporation sites along the steps; as a result, the density of incorporation sites depended on supersaturation.[13] We show that the chosen model system, rhombohedral R3 crystals of porcine insulin,[14] satisfies all three of the above requirements. Aside from adding to the very few protein

(1) Jackson, K. A. In *Growth and Perfection of Crystals*; Doremus, R. H., Roberts, B. W., Turnbull, D., Eds.; Chapman and Hill: London, 1958; pp 319−323.
(2) Chernov, A. A. *Sov. Phys. Uspekhi* **1961**, *4*, 116−148.
(3) Kossel, W. *Nachr. Ges. Wiss. Göttingen* **1928**, 135−138.
(4) Stranski, I. N. *Z. Phys. Chem.* **1928**, *136*, 259−278.
(5) Chernov, A. A. *Modern Crystallography III, Crystal Growth*; Springer: Berlin, 1984.
(6) Kaischew, R.; Stranski, I. N. *Z. Phys. Chem.* **1937**, *B35*, 427−432.
(7) Burton, W. K.; Cabrera, N.; Frank, F. C. *Philos. Trans. R. Soc. London Ser. A* **1951**, *243*, 299−360.

(8) Atkins, P. *Physical Chemistry*; 6th ed.; Freeman: New York, 1998.
(9) Markov, I. V. *Crystal Growth for Beginners. Foundations of Nucleation, Crystal Growth and Epitaxy*; World Scientific: Singapore, 1995.
(10) Williams, E. D.; Bartelt, N. C. *Science* **1991**, *251*, 393−400.
(11) Bales, G. S.; Zangwill, A. *Phys. Rev. B* **1990**, *41*, 5500−5508.
(12) Vekilov, P. G.; Alexander, J. I. D. *Chem. Rev.* **2000**, *100*, 2061−2089.
(13) Teng, H. H.; Dove, P. M.; Orme, C. A.; De Yoreo, J. J. *Science* **1998**, *282*, 724−727.

systems, the crystallization kinetics of which have been studied in detail,[15,16] insulin crystallization is of interest because it constitutes the main technological process in the production of several diabetes medications.[17,18]

Experimental Section

Preparation of rhombohedral Insulin Crystals. Porcine insulin (powder) was purchased from Sigma-Aldrich (St. Louis, MO; Lot numbers 012K1881, 102K1065) and used without further purification. A stock solution of the protein in 0.02 M HCl (Fisher, Fair Lawn, NJ) was prepared and filtered using Millipore Ultrafree-CL microcentrifuge filters with the molecular weight cut off of 30 kDa (Sigma-Aldrich, St. Louis, MO), and the absorbance at 276 nm was determined with a Beckman DU 68 spectrophotometer. The molar extinction coefficient of 6000 M^{-1} cm^{-1} [19] was used to calculate the protein concentration from the absorbance measurements.

Rhombohedral insulin crystals were grown using the protocol described in ref 14. In short, to an aliquot of insulin solution in 0.02 M HCl were added, in the order listed, 0.12 M zinc chloride (Sigma, St. Louis, MO), 0.2 M trisodium citrate (Fisher, Fair Lawn, NJ), neat acetone (SPLC-grade, Fisher, Fair Lawn, NJ), and water in a 1:5:3:1 volume ratio. Thus, the final concentrations of the components in the crystallizing solutions were as follows: insulin, between 0.75 and 5 mg mL^{-1}; $ZnCl_2$, 0.006 M; trisodium citrate, 0.05 M; acetone, 15%. In experiments where acetone was not used, it was replaced by 0.02 M HCl.

Atomic Force Microscopy (AFM). Metal disks used for mounting samples in the AFM (Veeco Metrology Group, Santa Barbara, CA) were coated with Teflon adhesive tape (BYTAC, Sigma, St. Louis, MO), following the procedure of ref 20. These were cleaned with 2% sodium dodecyl sulfate (SDS, Sigma, St. Louis, MO) and rinsed with copious amounts of water before each experiment. Then 10 μL drops of crystallizing solution were deposited directly on the Teflon-coated disks, covered with 16 mm glass Petri dishes, and sealed with Parafilm. Crystals with a characteristic rhombohedral shape typically appeared after an overnight incubation at 4 or 20 °C.

The Teflon-coated metal disks with the grown insulin crystals were mounted on a Nanoscope IIIa or a Nanoscope IV atomic force microscope (Vecoo Metrology Group, Santa Barbara, CA), equipped with a 120 μm ("J") scanner and a Tapping Mode fluid cell. The fluid cell, as well as the O-ring and tubing, if used, were washed with 2% SDS and copious amount of water before each experiment. The crystal was placed directly underneath the AFM tip with the aid of an optical microscope.[21] At no point during the setup were the crystals exposed to air.

In experiments performed in the absence of acetone, the fluid cell was sealed using an O-ring in order to ensure constant conditions during imaging. The use of the O-ring was found to be incompatible with acetone-containing buffer due to the formation of bubbles, likely of acetone vapor, inside the cell.

Images were acquired in buffer solutions of identical composition to the mother liquor (see above), but at various concentrations of insulin. Unless indicated otherwise, imaging was performed in the tapping mode. Oxide-sharpened silicon nitride tips mounted on cantilevers with nominal spring constants of ~0.06 N/m were used. Standard procedures for the microscope setup (frequency, driving voltage, and set point)

were followed.[22] The scanning parameters were adjusted so that continuous imaging did not affect the morphology of the imaged part of the surface, or the rate of the monitored processes. This was verified by varying the scan size and the time intervals between scans. For details on similar observations with apoferritin, see ref 23.

Solutions were exchanged using 1 mL syringes attached to the exchange ports of the fluid cell. At least 300 μL of fresh solution was flown through the cell to ensure complete exchange. The solution and the microscope were allowed to equilibrate for at least 2 h following the exchange of solutions or mounting of a new crystal.

Temperature in the fluid cell was monitored using a digital thermometer (HH506R from Omega Engineering, Stanford, CT) equipped with a K-type thermocouple. The thermocouple was attached to the top of the scanner next to the fluid cell but was not in contact with the solution during actual crystallization runs. A control determination, in which a second thermocouple attached to a second thermometer was immersed in the solution, found that the difference between the temperature in the fluid cell and the one read by the outside thermocouple was consistently ~0.5 °C. In all runs, the temperature in the crystallization solution was in the range 26.8–27.3 °C.

Determination of Step Growth Rate. For crystals growing slowly, such as ferritin or apoferritin, the step growth rates v can be determined by counting the number of molecules that attach to a step between two images. For fast growing crystals such as insulin, we apply the following two methods.

The first method involves choosing a scanning direction such that the steps are parallel to the slow scan axis and disabling scanning along this axis. The y-axis of the acquired pseudo-image then becomes the time axis, and v is determined from the distance traveled by the step in the x (fast scan axis) direction for a certain time interval.[24]

The second method involves acquiring the up-scan and down-scan area images of the step train and measuring the angles that the steps make with the fast scan axis. The step velocity is then calculated from the two angles θ_D and θ_U as[25]

$$v = \frac{FW}{2N}(\cot\theta_D - \cot\theta_U)\sin\left[\cot^{-1}\left(\frac{\cot\theta_D + \cot\theta_U}{2}\right)\right] \quad (1)$$

where F is the scan rate in lines per second, W is the scan size, and N is the number of scan lines in an image.

If the steps move so fast that those imaged during an up-scan are different from those imaged during a down-scan, this method is only applicable to cases where step density is constant or step velocity does not depend on step density. The first method is more general and is free of this limitation.

Determination of the Crystallization Driving Force. The crystallization driving force, or supersaturation, is written as

$$\sigma = \{\exp[-(\mu_c - \mu_s)/k_BT] - 1\} \quad (2)$$

where

$$\mu_s = \mu_0 + k_BT\ln(\gamma C) \text{ and } \mu_c = \mu_0 + k_BT\ln(\gamma_e C_e) \quad (3)$$

In these expressions, subscripts c and s denote crystal and solute, respectively, C and n are, respectively, the protein mass and molecular concentrations, $n = C/m$, and $m = M_{insulin}/N_{Avogadro} = 6.6 \times 10^{-20}$ g is the mass of the insulin hexamer; the subscript e indicates their values at equilibrium with the crystal.

(14) Harding, M. M.; Hodgkin, D. C.; Kennedy, A. F.; O'Connor, A.; Weitzmann, P. D. J. *J. Mol. Biol.* **1966**, *16*, 212–226.
(15) McPherson, A.; Malkin, A.; Kuznetsov, Y.; Plomp, M. *Acta Crystallogr., Sect. D* **2001**, *57*, 1053–1060.
(16) Vekilov, P. G.; Chernov, A. A. In *Solid State Physics*; Ehrenreich, H., Spaepen, F., Eds.; Academic Press: New York, 2002; Vol. 57, pp 1–147.
(17) Brange, J. *Galenics of Insulin*; Springer: Berlin, 1987.
(18) Schlichtkrull, J. *Acta Med. Scandin.* **1965**, *177*, 103–113.
(19) Pace, N. C.; Vajdos, F.; Fee, L.; Grimsley, G.; Gray, T. *Protein Sci.* **1995**, *4*, 2411–2423.
(20) Müller, D. J.; Amrein, M.; Engel, A. *J. Struct. Biol.* **1997**, *119*, 172–188.
(21) Yip, C. M.; DePhelippis, M. R.; Frank, B. H.; Brader, M. L.; Ward, M. D. *Biophys. J.* **1998**, *75*, 1172–1179.

(22) Hansma, P. K.; Cleveland, J. P.; Radmacher, M.; Walters, D. A.; Hillner, P.; Bezanilla, M.; Fritz, M.; Vie, D.; Hansma, H. G.; Prater, C. B.; Massie, J.; Fukunaga, L.; Gurley, J.; Elings, V. *Appl. Phys. Lett.* **1994**, *64*, 1738–1740.
(23) Yau, S.-T.; Petsev, D. N.; Thomas, B. R.; Vekilov, P. G. *J. Mol. Biol.* **2000**, *303*, 667–678.
(24) Lin, H.; Petsev, D. N.; Yau, S.-T.; Thomas, B. R.; Vekilov, P. G. *Cryst. Growth Des.* **2001**, *1*, 73–79.
(25) Land, T. A.; DeYoreo, J. J.; Lee, J. D. *Surf. Sci.* **1997**, *384*, 136–155.
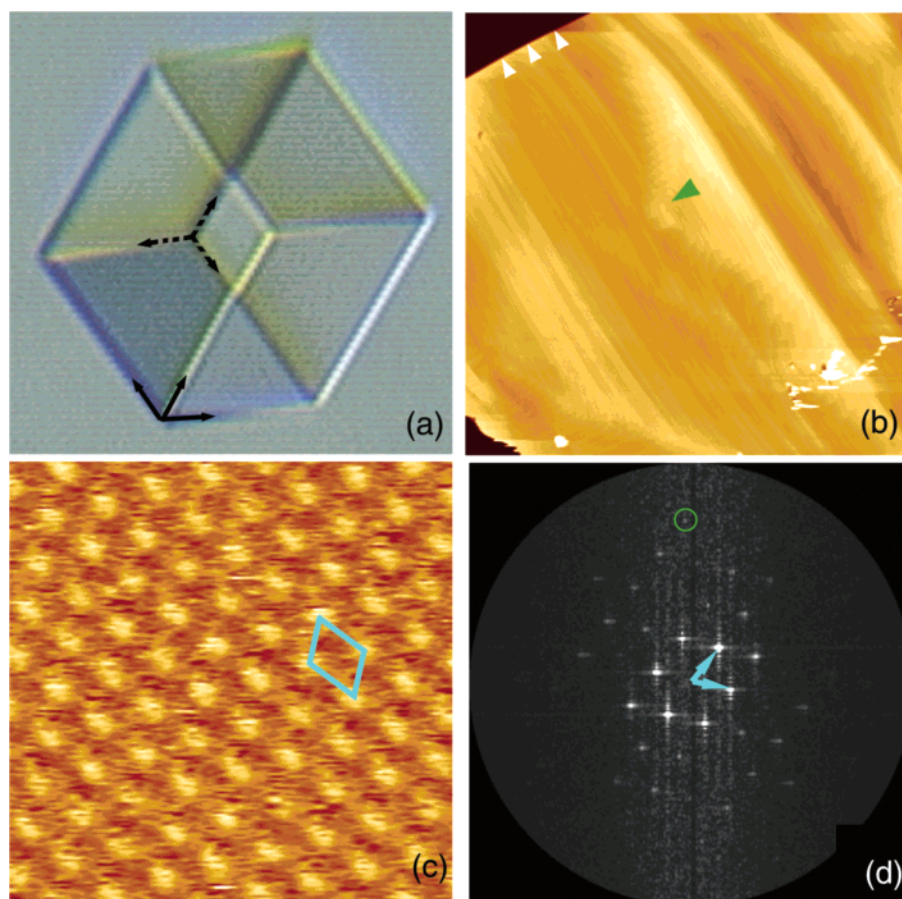
Figure 1. Rhombohedral (R3) insulin crystals. (a) An optical micrograph of a typical rhombohedral insulin crystal used in this study. The edge of a crystal is ~200 μm. Black solid arrows mark the bottom corner closest to the observer. Black dashed arrows mark the bottom corner furthest from the observer. (b) A 35×35 μm^2 (Z-scale: 0.3 μm) tapping mode AFM image of the surface of a crystal, such as the one shown in (a), grown in the absence of acetone. The green arrowhead points to a dislocation outcrop. The white arrowheads point to the edge of the crystal. $\sigma = (C - C_e)C_e^{-1} = 3$. (c) A 57×57 nm^2 (Z-scale: 5 nm) contact mode AFM image acquired on a terrace of the growing face of an insulin crystal. A 2D unit cell is indicated in turquoise. (d) A Fourier transform of the image shown in (c). A $(-3,4)$ reflection at 1.7 nm resolution is encircled in green, and hk basis vectors are indicated with turquoise arrowheads.

The solubility C_e of insulin was determined from the intercept of the dependence of the step growth rate on the protein concentration with the abscissa. In the presence of acetone $C_e = 0.11 \pm 0.02$ mg mL^{-1}, in the absence of acetone $C_e = 0.15 \pm 0.02$ mg mL^{-1}. Furthermore, in both cases, it was observed that the growth steps retreat at concentrations $C < C_e$. The datum point without acetone equals the result on an independent determination of the solubility of insulin crystals (L. Bergeron et al., in preparation). The value of C_e in the presence of acetone was used to determine the concentration of this volatile cosolvent during the AFM monitoring—this C_e value corresponds to the solubility in the presence of 5% acetone, and we conclude that this is the residual concentration of acetone in those runs.

The activity coefficients γ and γ_e were evaluated according to the relationship $\ln \gamma = 2B_2M_{insulin}C$.[23,26] While data concerning the second virial coefficient B_2 for insulin are not available, we note that for proteins under crystallizing conditions B_2 is always negative and the maximum magnitude on record is 8×10^{-4} cm^3 mol g^{-2}.[27–29] For $C <$ 1 mg mL$^{-1} = 10^{-3}$ g cm^{-3}, and $C_e \sim 10^{-4}$ g cm^{-3}, the assumption $\gamma \approx \gamma_e \approx 1$ yields at most 3% bias in the value of σ evaluated as $(C/C_e - 1) = (n/n_e - 1)$.

High-Resolution AFM Imaging and Comparison with the X-ray Data. To test if the observed crystals were of rhombohedral form, high-resolution images were acquired from areas on the terraces between the steps of the habit-forming faces. Contact mode and an open fluid cell (without the O-ring) were used. Images were processed using GRIP (for Groningen Image Processing) software package (http://rugbe2.chem.rug.nl/software.htm) on a dedicated Linux workstation using standard Fourier analysis methods.

For the purposes of comparing the observed lattice with that expected on the basis of the X-ray diffraction study, the 2 Zn insulin structure (pdb code 4INS[30]) was imported into the Swiss PDB viewer, version 3.7b2.[31] The structure of the (100) face was generated by applying a set of standard R3 symmetry operators and translations along crystallographic axes to position the molecules at the desired locations.

Results and Discussion

Rombohedral (R3) Insulin Crystals. Under the conditions employed in this study, porcine insulin crystallizes almost exclusively in the rhombohedral (R3) form.[14] Correspondingly, all crystals that we saw had the typical rhombohedral shape, Figure 1a. Even small crystals (~10–20 μm in size) were firmly

(26) Hill, T. L. *Introduction to Statistical Thermodynamics*; Dover: New York, 1986.

(27) George, A.; Wilson, W. W. *Acta Crystallogr., Sect. D* **1994**, *50*, 361−365.

(28) Guo, B.; Kao, S.; McDonald, H.; Wilson, W. W.; Asanov, A.; Combs, L. L. *J. Cryst. Growth* **1999**, *196*, 424−433.

(29) Rosenbaum, D. F.; Zamora, P. C.; Zukoski, C. F. *Phys. Rev. Lett.* **1996**, *76*, 150−153.

(30) Baker, E. N.; Blundell, T. L.; Cutfield, J. F.; Cutfield, S. M.; Dodson, E. J.; Dodson, G. G.; Crowfoot-Hodgkin, D. M.; Hubbard, R. E.; Isaacs, N. W.; Reynolds, C. D.; Sakabe, K.; Sakabe, N.; Vijayan, N. M. *Philos. Trans. R. Soc. London* **1988**, *B319*, 369−456.

(31) Guex, N.; Peitsch, M. C. *Electrophoresis* **1997**, *18*, 2714−2723.

attached to the Teflon substrate. The orientation of the crystals was random, indicating that the crystals either nucleated on the rough Teflon surface or, if homogeneously nucleated in the solution bulk, attached at an early stage while their sizes were smaller than the lengthscales of the roughness of the Teflon substrate.

The lattice parameters of the rhombohedral R3 form of porcine insulin are $a = 4.9$ nm, $\alpha = 114.8°$ (rhombohedral setting), or $a = 8.25$ nm, $c = 3.4$ nm (hexagonal setting).[30] The crystal habit is defined by the planes with indexes {100} (rhombohedral system) or {10$\bar{1}$1} (hexagonal system), which exhibited steps and numerous dislocation outcrops (Figure 1b). The molecules on the surface of {100} faces can be viewed as occupying lattice sites on a 2D lattice with parameters $a = b = 4.9$ nm, $\alpha = 114.8°$ (this angle is usually referred to as γ; α is used here to avoid confusion with surface free energy. Furthermore, for ease of comparison with the X-ray data, a lattice with $a = b$ is chosen).[30]

A high-resolution contact mode AFM image of the (100) face is shown in Figure 1c. Such images were acquired with the solution held by surface free energy in a liquid bridge between the substrate and the top of the fluid cell, i.e., in the absence of the O-ring, to avoid image distortions associated with its use.[32,33] The image in Figure 1c can be characterized by a 2D lattice with $a = 6.8 \pm 0.2$ nm, $b = 6.3 \pm 0.1$ nm, $\alpha = 115.4 \pm 0.5°$ (Figurse 1c,d). The ~23−28% stretching of the observed lattice relative to the X-ray structure was traced to a scanner calibration error. After recalibration, the parameters determined from other similar images were $a = 4.7 \pm 0.2$ nm, $b = 4.7 \pm 0.1$ nm, $\alpha = 117.9 \pm 0.5°$. Images with resolution of up to 1.2 nm, as determined from their Fourier transforms (such as one shown in Figure 1d), were acquired (not shown). The details of the surface structure of the insulin hexamer will be addressed elsewhere.

Anisotropy of Step Growth Kinetics. Figure 2 shows examples of growth steps spiraling around single, in (a), and multiple, in (b), screw dislocations. The spirals form hillocks shaped as tetragonal pyramids with parallelogram bases, consisting of steps moving in $\langle 010 \rangle$ and $\langle 001 \rangle$ directions. The side faces of the growth pyramids are referred to as vicinals. To orient the surface coordinate system with respect to the crystallographic coordinates, we use the observation that the steps are parallel to crystal's edges. The direction of step motion on the vicinal with lowest step density is labeled as [010] and on the vicinal to its right as [001]. On images acquired in the absence of the O-ring (not shown), the angle between steps generated by a dislocation was found to be $116 \pm 3°$, close to the value of $\alpha = 114.8°$ expected from the crystallographic data. Thus, we conclude that the steps are oriented along the molecular rows in the crystal. The polygonal shape of the spiral reflects the anisotropy of the step growth kinetics—they are significantly faster in the $\langle 011 \rangle$ directions, pointing toward the corners of the parallelogram, than in the $\langle 010 \rangle$ and $\langle 001 \rangle$ directions. This is attributed to the weaker hexamer−hexamer bonds along the latter directions. The absence of the {111} faces from the crystal habit implies that the hexamer−hexamer bonds responsible for the stacking of hexamers along the three-fold axis (the [111]

(32) Reviakine, I.; Bergsma-Schutter, W.; Brisson, A. *J. Struct. Biol.* **1998**, *121*, 356−362.
(33) Neff, G. A.; Gragson, D. E.; Shon, D. A.; Baker, S. M. *Langmuir* **1999**, *15*, 2999−3002.
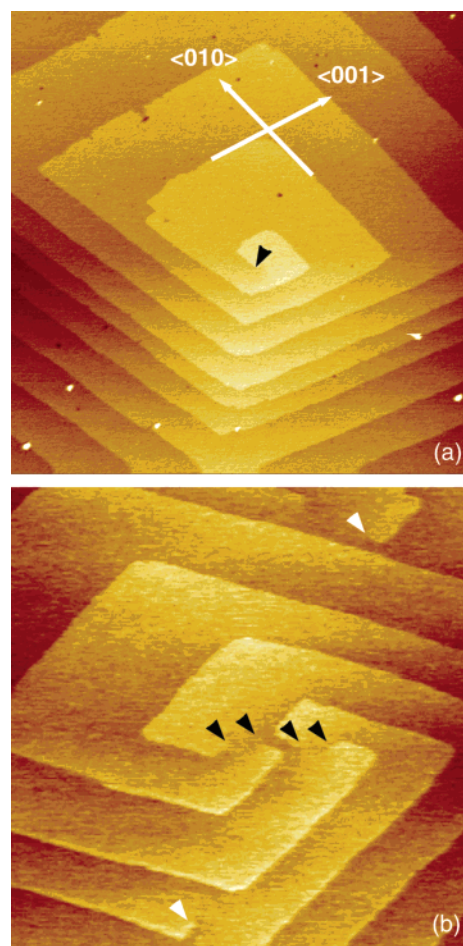
Figure 2. Two-dimensional anisotropy of growth on the (100) face of insulin. (a) Growth hillock around a single dislocation. Density of steps in [010] and [001] directions is approximately double the step density in [0$\bar{1}$0] and [00$\bar{1}$] directions. Image size 6.4 μm. Z-scale 50 nm. $\sigma = 0.8$ (b) Growth hillock around four dislocations, indicated with black arrowheads, that work in cooperation to produce a hillock, with two dislocations, indicated with white arrowheads, on the hillock side. Image size 3.0 μm. Z-scale 30 nm. $\sigma = 0.8$.

direction) are significantly stronger than those in the $\langle 011 \rangle$, $\langle 010 \rangle$, and $\langle 001 \rangle$ directions.

In general, the differences between the interstep distances l in the [010], [001], [0$\bar{1}$0], and [00$\bar{1}$] directions reflect the anisotropy of the step growth rate v_i.[5] The distance between two adjacent steps in each direction l_i

$$l_i = v_i \tau \tag{4}$$

where τ, the rotation period of the spiral, in general, does not depend on the step orientation since it is linked to the face growth rate R via

$$R = h/\tau \tag{5}$$

(h − step height). Thus, the shape of the hillock reveals the anisotropy of the step growth rate and of the respective step kinetic coefficients β_i, defined from[2,5]

$$v_i = \beta_i \Omega C_e \sigma \tag{6}$$

where $\Omega = 11125$ Å^3 [30] is the volume that one molecule occupies in the crystal.

Figure 2a shows that the step density on all four vicinals varies with distance from the dislocation. In some cases, the areas of varying step density on different vicinals occur at the same spiral turn. These are likely caused by faster spiral rotation due to an upward fluctuation of the interfacial supersaturation at the dislocation outcrop. In other cases, areas of low step density on a particular vicinal are likely caused by an upward fluctuation of the interfacial supersaturation around the particular steps leading to their faster growth. These latter fluctuations lead to deviations from the general rules formulated above and affect the hillocks' shape and the ratios between the step−step distances. Measurements of the step−step distances on various vicinals lead to the statistically significant anisotropy of the step kinetic coefficients β_i and the step−step distances l_i of

$$l_{[010]}/l_{[001]}/l_{[001]}/l_{[00\bar{1}]} = \beta_{[010]}/\beta_{[001]}/\beta_{[001]}/\beta_{[00\bar{1}]} \approx 1.5/1/1/1 \tag{7}$$

in the absence of acetone and

$$l_{[010]}/l_{[001]}/l_{[001]}/l_{[00\bar{1}]} = \beta_{[010]}/\beta_{[001]}/\beta_{[001]}/\beta_{[00\bar{1}]} \approx 1.5/1.5/1.5/1$$

in its presence.

Kinetics of Step Propagation. Figure 3a,b show examples of trains of growth steps. For all imaged steps, the step height had a distribution centered at $h = 3.4 \pm 1$ nm, the layer thickness determined from the X-ray crystal structure.[30] The width of this distribution reflects the molecular lengthscale roughness of the steps.

Figure 3a shows a step train with relatively uniformly spaced steps, an arrangement typical of the majority of the observations, with or without acetone. In several cases, mostly in the absence of acetone, we saw step trains with nonuniform step density, such as the one in Figure 3b. The nonuniform density allows us to extract dependences of the step velocity v on interstep distance l. In Figure 3d three such dependencies are shown with respect to the slope of the respective vicinal $p = h/l$. We see that the step velocity is independent of step density for slopes as high as 3×10^{-2}, indicating that steps as close as ~100 nm do not interact. Below, we show that steps separated by $l <$ 100 nm are slowed, likely due to overlapping fields of supply via surface diffusion.[25,34−36]

The step velocity v was found to be a linear function of supersaturation σ, Figure 3e. The step kinetic coefficients for the fast vicinals extracted from linear regression fits to the data in Figure 3f are $\beta = 7 \times 10^{-3}$ cm s^{-1} for growth without acetone and 4×10^{-2} cm s^{-1} in the presence of ~5% acetone.

The values of the kinetic coefficient β, the prevalent vicinal slope during crystallization $p \sim 10^{-2}$, and the diffusion coefficient of the protein $D = 8 \times 10^{-7}$ cm^2 s^{-1}[37] are used to evaluate the kinetic Peclet number $Pe_k = \beta p \delta / D$[38] by using a value of the characteristic thickness of the diffusion layer $\delta \sim 2 \times 10^{-2}$ cm (a low estimate, stemming from a direct determination and an evaluation in simulations of the convective-diffusive transport with lysozyme,[39,40] a crystal growing under kinetic control for which one would expect a shorter δ). This coefficient emerges from the analysis of stability of

equidistant step trains,[41] such as the one in Figure 3a, and characterizes the relative weight of the kinetics of incorporation of the molecules into the crystal with respect to those of their transport through solution. Extreme values ($\ll 1$ or $\gg 1$) of Pe_k are characteristic of systems, controlled by either the kinetics of incorporation of molecules into the crystal, $Pe_k \ll 1$, or transport of molecules through the solution, $Pe_k \gg 1$. Random fluctuations in such systems decay rapidly and equidistant trains of noninteracting steps remain stable.[42] Intermediate values are indicative of comparable rates of transport and incorporation and characterize systems that are intrinsically unstable to step density fluctuations, irrespectively of whether steps interact with each other or not.

Insulin crystallization is characterized by very high values of Pe_k of 1.6 and 8, Table 1, signifying that the kinetics of crystallization are transport-controlled. Thus, in contrast to many other protein systems,[12,43] in insulin crystallization bunching of steps is *not an intrinsic* feature of the step trains—equidistant step trains are the stable mode of growth.[44] The observed step bunches (Figure 3b) were always caused by unsteady generation of new layers by two-dimensional nucleation at the block boundaries of crystals consisting of several blocks, as discussed in the following subsection.

Another consequence of the transport-controlled crystallization kinetics is the likely possibility that the interfacial hexamer concentration is lower than the bulk C,[24] used in the plots in Figure 3e, due to depletion at the interface. Since we cannot quantitatively account for this phenomenon, we use the kinetic coefficients determined using the bulk concentrations, keeping in mind that their values represent lower limits on the actual β's.

The summary of the known kinetic coefficients for protein growth in Table 1 reveals that these are by far the highest values recorded to date and are comparable to the values for inorganic systems. This fact suggests that slow kinetics are not a general feature of protein crystallization and only occur with some proteins, and may help us understand the factors governing the kinetics of protein crystallization.

As with ferritin and apoferritin,[23,45,46] a linear $v(\sigma)$ dependence suggests high density of incorporations sites, kinks, between straight step segments, along the steps. The molecular-resolution image of the step edge shown in Figure 3e shows that this is indeed the case. The steps are very rough with straight segments consisting of, on the average, less than two molecules.

To summarize, the kinetics of step motion are free of complicating factors: (i) high density of incorporation sites along the molecularly rough steps provides for linear step growth kinetics; (ii) the lack of step−step interactions at the typical separations between the steps ensures that the step kinetics are not affected by the step separation; (iii) the transport control of growth provides for dissipation of the step density fluctuations

(34) Sato, M.; Uwaha, M. *Phys. Rev. B* **1995**, *51*, 11172−11181.
(35) Uwaha, M.; Saito, Y.; Sato, M. *J. Cryst. Growth* **1995**, *146*, 164−172.
(36) Vekilov, P. G.; Rosenberger, F. *J. Cryst. Growth* **1996**, *158*, 540−551.
(37) Hvidt, S. *Biophys. Chem.* **1991**, *39*, 205−213.
(38) Vekilov, P. G.; Thomas, B. R.; Rosenberger, F. *J. Phys. Chem.* **1998**, *102*, 5208−5216.

(39) Pusey, M.; Witherow, W.; Naumann, R. *J. Cryst . Growth* **1988**, *90*, 105−111.
(40) Lin, H.; Rosenberger, F.; Alexander, J. I. D.; Nadarajah, A. *J. Cryst . Growth* **1995**, *151*, 153−162.
(41) Vekilov, P. G.; Alexander, J. I. D.; Rosenberger, F. *Phys. Rev. E* **1996**, *54*, 6650−6660.
(42) Vekilov, P. G.; Rosenberger, F. *Phys. Rev. Lett.* **1998**, *80*, 2654−2656.
(43) Lin, H.; Yau, S.-T.; Vekilov, P. G. *Phys. Rev. E* **2003**, *67*, 0031606.
(44) Gliko, O.; Reviakine, I.; Vekilov, P. G. *Phys. Rev. Lett.* **2003**, *90*, 225503.
(45) Yau, S.-T.; Thomas, B. R.; Vekilov, P. G. *Phys. Rev. Lett.* **2000**, *85*, 353−356.
(46) Petsev, D. N.; Chen, K.; Gliko, O.; Vekilov, P. G. *Proc. Natl. Acad. Sci. U.S.A.* **2003**, *100*, 792−796.
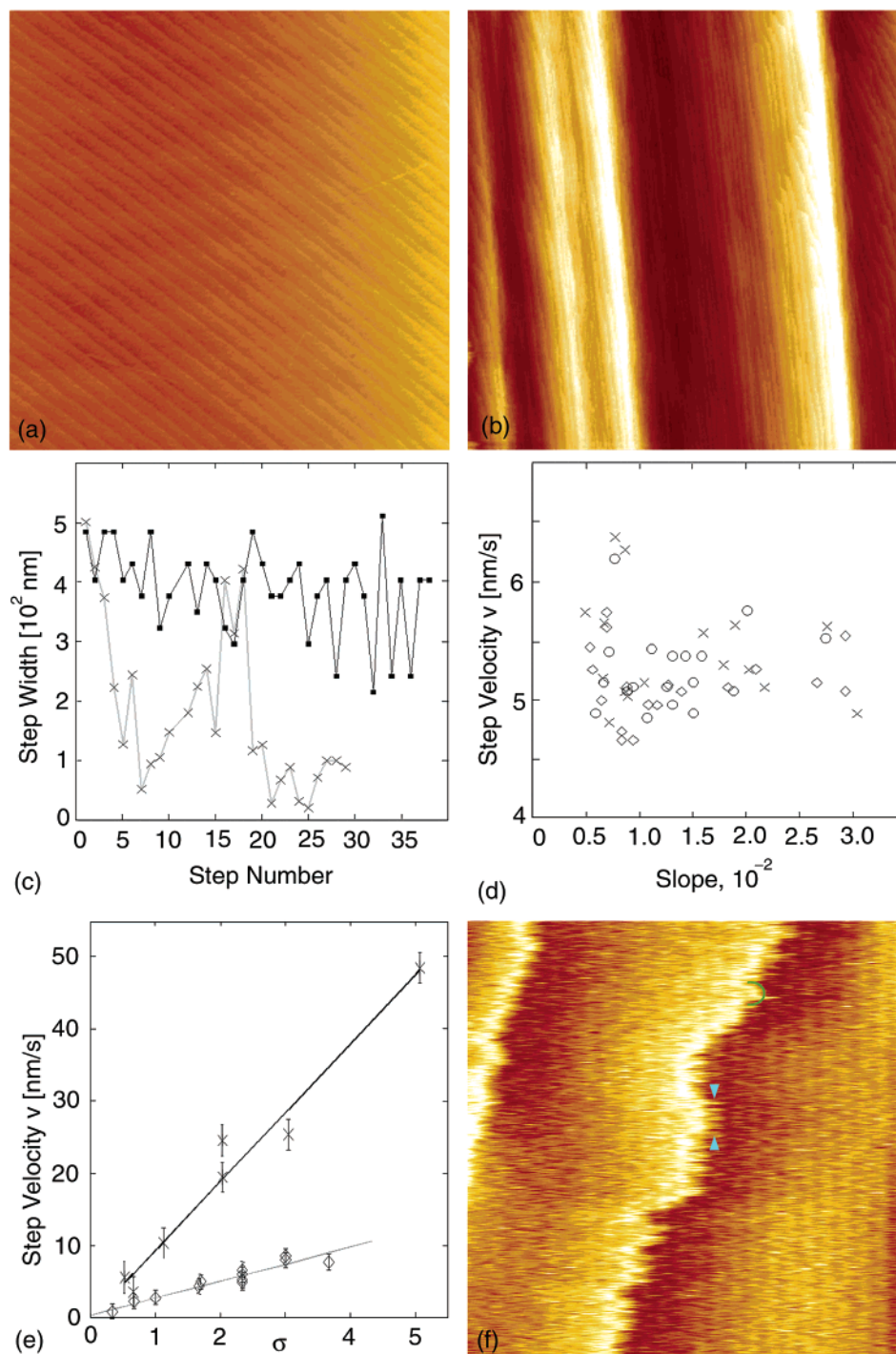
Figure 3. Step velocity, step density, and step−step interactions. (a) A train of equidistant parallel steps. Image size 11 μm, Z-scale 120 nm, supersaturation $\sigma = (C - C_e)C_e^{-1} = 0.75$, where C is protein concentration and C_e is its solubility. Steps are moving from the lower left corner, which is higher, to the lower right corner, which is lower. (b) A train of parallel steps with a nonuniform step density (areas of high step density are called step bunches). Image size 20 μm. Z-scale 75 nm. Supersaturation $\sigma \approx 3$. Steps are moving from left to right. (c) Quantification of the variations of step widths in (a) black line/solid squares and (b) gray lines/crosses. (d) The dependence of the step velocity on the slope of the step train $p = hl^{-1}$ (h, step height ; l, step width); three independent sets of measurements show no correlation. The higher scatter in the velocity measurements at smaller slope values is due to the greater number of data points in that region. $\sigma = 1.7$. (e) Step velocity as a function of supersaturation $\sigma = (C - C_e)C_e^{-1}$, in the presence (crosses) and in the absence (open symbols) of acetone. Lines are regression fits to the respective sets of data. (f) Molecular resolution image of the step edge illustrating its molecular-scale roughness. The fuzzy appearance of the molecules at the edge is caused by the attachment/detachment events characteristic of an equilibrium process such as step advancement (turquoise daggers) Semicircle highlights one of the molecules. The absence of imaging artifacts was verified immediately after this image was collected by scanning a larger area including the area imaged here. Image size 250 nm. Z-scale 9 nm, $\sigma = 0.8$.

and stable equidistant step trains, from which the characteristic step spacing can be determined. The simplicity of the step kinetics allows unambiguous identification of the thermody-

namic factors that play a role in the determination of the overall rate of crystallization.

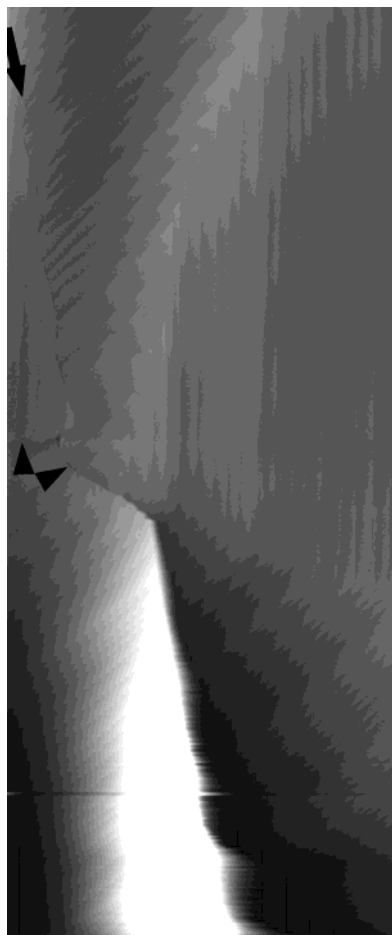**Enhanced Two-Dimensional Nucleation at Gross Lattice**

Figure 4. Junction of three blocks boundaries at $\sigma = 1.667$. The steps do not cross the block boundaries. The steps at the lower block at the right are generated at variable rate at two locations near the triple junction. Image size 10.4×25 μm. Z-scale 0.25 μm.

Table 1. Kinetic Coefficient, β, Diffusivities, D, and Peclet Coefficients, Pe_k, for Various Systems. Local Slope Was Assumed To Be $\sim 10^{-2}$ unless Indicated Otherwise

system	β [cm s^{-1}]	D [cm^2 s^{-1}]	Pe_k	source
R3 porcine insulin				this work
no acetone	7×10^{-3}	7.9×10^{-7}	1.6	
$\sim 5\%$ acetone	4×10^{-2}		8	
apoferritin	6×10^{-4}	3.2×10^{-7}	0.7	45
ferritin	6×10^{-4}	3.2×10^{-7}	0.7	46
canavalin, R3 form	$(5.8-26) \times 10^{-4}$	4×10^{-7}	1–4	25
catalase	3.2×10^{-5}			57
lysozyme {101}				
typical	$(2-3) \times 10^{-4}$	7.3×10^{-7}	0.05	58
no step bunching	2×10^{-3}		0.3	38
lysozyme {110}	$(2-3) \times 10^{-4}$			36
STMV	$(4-8) \times 10^{-4}$	2×10^{-7}	1.2	59
thaumatin	2×10^{-4}	6×10^{-7}	0.1	60
various inorganic systems (ADP, KDP, alums, etc.)	$\sim 10^{-2}-10^{-1}$	$\sim 10^{-6}$		16

Defects. To identify the cause of the step bunches that were sometimes observed during crystallization, we panned the AFM viewfield toward the source of the step. We found that the steps were generated at a variable rate at the outcrop line of block boundaries on the crystal surface, where the lattice misfit in a direction perpendicular to the monitored face creates a step. As Figure 4 illustrates, new steps are generated on the surface of the lower block by 2D nucleation—this layer generation mode is enhanced at the concave angle of the step.[47]

Sometimes, the defects causing the generation of nonuniform

step trains are not apparent in solutions of moderate or high supersaturation. However, as the protein concentration is lowered below a certain supersaturation, molecules (in the case of insulin, hexamers) located at the defects leave the crystal due to their higher activity. In this way, we detect previously hidden defects, such as those shown in Figure 5a,b.

Since dissolution is also enhanced around the dislocation due to their own strain field, we need to distinguish between the dissolution fingerprint of block boundaries and dislocations. An etch pit with a distinct inverted pyramid shape forms around the dislocation line as the spiral unwinds and is shown in Figure 5c.

Step Interactions at Short Separations. A group of several screw dislocations, imaged over a period of ~ 6 min at ~ 50 s intervals, is shown in Figure 6. The multiwing spiral produced by such dislocations exhibits the polygonal shape visible in Figure 2.

The steps remain straight and unaffected by each other's presence down to a distance of $l < 100$ nm (~ 17 molecules) between each other, indicating that the characteristic length of the diffusion fields of the steps λ_s is ≤ 50 nm. We also note that for steps in step trains the separation from the respective dislocation outcrop points increases, e.g., between Figure 6c,d by ~ 260 nm, corresponding to a $v \approx 5$ nm/s, as in Figure 3e at $\sigma = 3$. The highlighted pair of steps moving against each other in the same two frames cover roughly the same distance, without completely merging in Figure 6d, i.e., their average velocity is about half of that of stand alone steps. Furthermore, we note several examples in Figure 6a–f of pairs of opposing steps separated by $\sim 50-100$ nm. These two observations suggest that at $l < 100$ nm the steps slow one another down. The strength of this interaction suggests, in analogy to other studied protein systems,[25,48,49] that the likely cause for the interaction is overlapping of the surface supply fields of the steps with characteristic length of $\lambda_s \sim 50$ nm.

Note that these interactions are of sufficiently short range so as not to affect the typical step trains with step separations of the order of 0.5 to 3 μm.

Generation of Steps at Screw Dislocations. Screw dislocations, shown in Figure 2 and Figure 6, were the dominant source of steps on the surfaces of porcine insulin crystals, consistent with a previous observation.[21] No evidence of normal growth modes was found under the conditions employed in this study. 2D nucleation only occurred if facilitated by a surface step created by block boundaries. Occasionally, 3D aggregates were seen on the crystal surface. Once these were attached strongly enough to be imaged, steps, and occasionally screw dislocations, were visible on their surfaces (not shown). It was therefore not possible to ascertain whether these were microcrystals sedimenting on the crystal's surface or liquid droplets, as suggested in.[50] Such objects were more often observed in the absence of acetone than in its presence, and in either case, at higher supersaturations.

Due to the lower supersaturation around small phases, the so-called Gibbs–Thomson (Kelvin) effect,[8,9] the growth of a

(47) Ming, N.; Tsukamoto, K.; Sunagawa, I.; Chernov, A. A. *J. Cryst. Growth* **1988**, *91*, 11−19.
(48) Vekilov, P. G.; Monaco, L. A.; Rosenberger, F. *J. Cryst. Growth* **1995**, *156*, 267−278.
(49) Chen, K.; Vekilov, P. G. *Phys. Rev. E* **2002**, *66*, 021606.
(50) Kuznetsov, Y. G.; Malkin, A. J.; McPherson, A. *Phys. Rev. B* **1998**, *58*, 6097−6103.
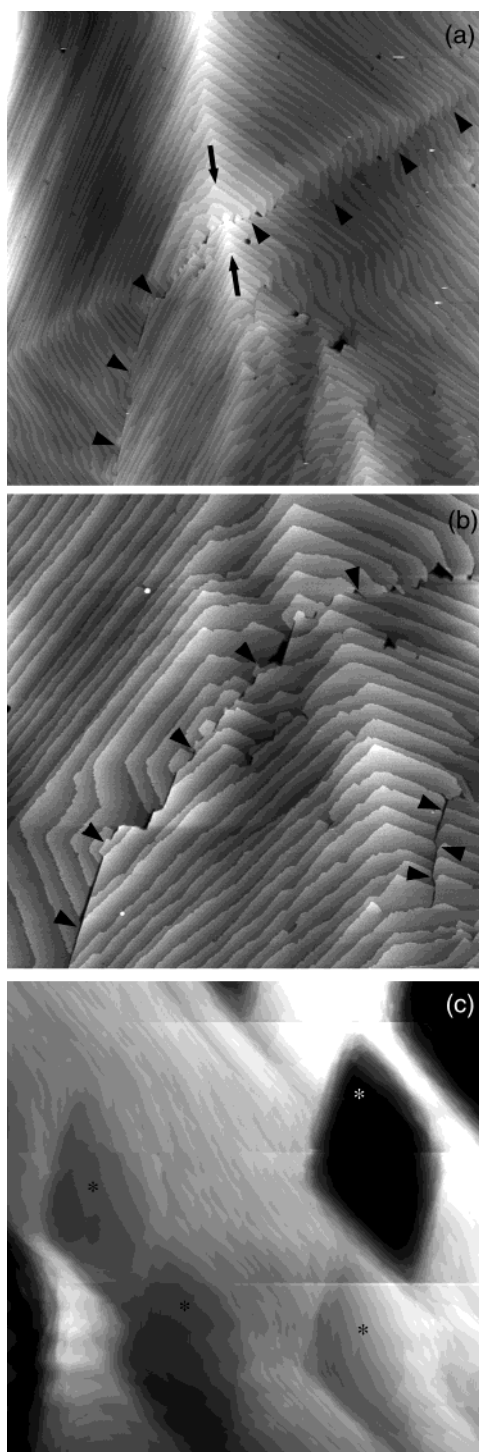
Figure 5. Defects observed in the crystals. (a) Grain boundary, indicated with black arrowheads, becomes visible as the concentration in solution approaches solubility due to preferential dissolution of the high-strain, high chemical potential, area of the defect. The ridge indicated with a black arrow shifts perpendicular to its direction when it crosses the boundary. Image size 15.8 μm. Z-scale 0.191 μm. $\sigma = 0.46$. (b) The defect shown in (a), 22 min later. The gap separating the blocks is visibly larger. Another defect, indicated with black arrowheads, is visible in the lower right corner of the image. Image size 5 μm. Z-scale 0.07 μm. (c) Etch pits (indicated with asterisks) appear as the dislocation spirals unwind. Image size: 17 μm. Z-scale 0.3 μm. This image was taken in buffer without insulin.

new segment of a polygonal spiral is not expected until it reaches, due to the growth of the preceding segments, the critical length L_c. This L_c is equal to the length of the respective edge

of the critical two-dimensional nucleus[51] and, in a system with rhombic symmetry, is related to the radius of an inscribed circle ρ_c as $\rho_c = L_c/2 \cdot \sin(\pi - \alpha)$, where α is the crystallographic angle. The critical ρ_c is defined by a 2D analogue of the Laplace relation

$$\rho_c = s\,\gamma_l/\Delta\mu \qquad (8)$$

where s is the surface area occupied by an insulin molecule, γ_l is the line tension of the step edge, and $\Delta\mu = \mu_c - \mu_s$ is the change in the insulin chemical potential upon transfer from solution into crystal.

In Figure 6, we illustrate the determination of L_c by in situ, real time AFM monitoring of the spiral rotation for several sources by the method described in.[13] The L_c values are summarized in Table 2. The large scatter of the data for the average L_c's is due to the fluctuations in the measured values (Figure 6h). These fluctuations are not the result of scanning artifacts, see Figure 6g, or of the finite frequency of image capture—finite sampling frequency may distort the intrinsic frequency of an object only if the monitoring frequency is lower. Figure 6a–f shows that image capture frequency is higher than the frequency of rotation of the spiral. Thus, we attribute the scatter in L_c to fluctuations of the interfacial supersaturation. Such fluctuations are likely for systems growing under strong transport control. A theoretical analysis using kinetic coefficients and diffusivities typical of protein crystallization systems and similar to those of insulin predicts periods of such fluctuations to be in the range of $100-1000$ s for proteins with diffusivities $<10^{-6}$ cm^2 s^{-1}.[52,53] Since the supersaturation fluctuations are random and local, no correlation between the fluctuations of L_c's at different locations on the face were observed. Furthermore, the interfacial supersaturation fluctuates around a characteristic mean value determined by the coupling of the transport processes and the incorporation kinetics. At low fluctuation amplitudes, eq 8 predicts a linear response of L_c to σ. This allows us to consider the mean L_c as the characteristic value at the given supersaturation.

As proposed in ref 51, the period of rotation τ of a tetragonal polygonal spiral consists of the four intervals that the step takes to travel the sides of the polygon $L_{c,i}$, $i = 1, 2, 3, 4$, with velocities v_i.

$$\tau = L_{c,1}\sin(\pi - \alpha_1)/v_1 + L_{c,2}\sin(\pi - \alpha_2)/v_2 + L_{c,3}\sin(\pi - \alpha_3)/v_3 + L_{c,4}\sin(\pi - \alpha_4)/v_4 \quad (9)$$

The distance between adjacent steps l on the ith vicinal

$$l_i = v_i\tau = \beta_i\left(\frac{L_{c,1}}{\beta_1}\sin(\pi - \alpha_1) + \frac{L_{c,2}}{\beta_2}\sin(\pi - \alpha_2) + \frac{L_{c,3}}{\beta_3}\sin(\pi - \alpha_3) + \frac{L_{c,4}}{\beta_4}\sin(\pi - \alpha_4)\right) \quad (10)$$

where α_i is the angle between the normal to the step and the respective side of the critical polygon.

(51) Kaischew, R.; Budevski, E. *Contemp. Phys.* **1967**, *8*, 489−516.
(52) Wang, M.; Liu, X.-Y.; Sun, C.; Ming, N.-b.; Bennema, P.; Enckevort, W. J. P. v. *Europhys. Lett.* **1998**, *41*, 61−66.
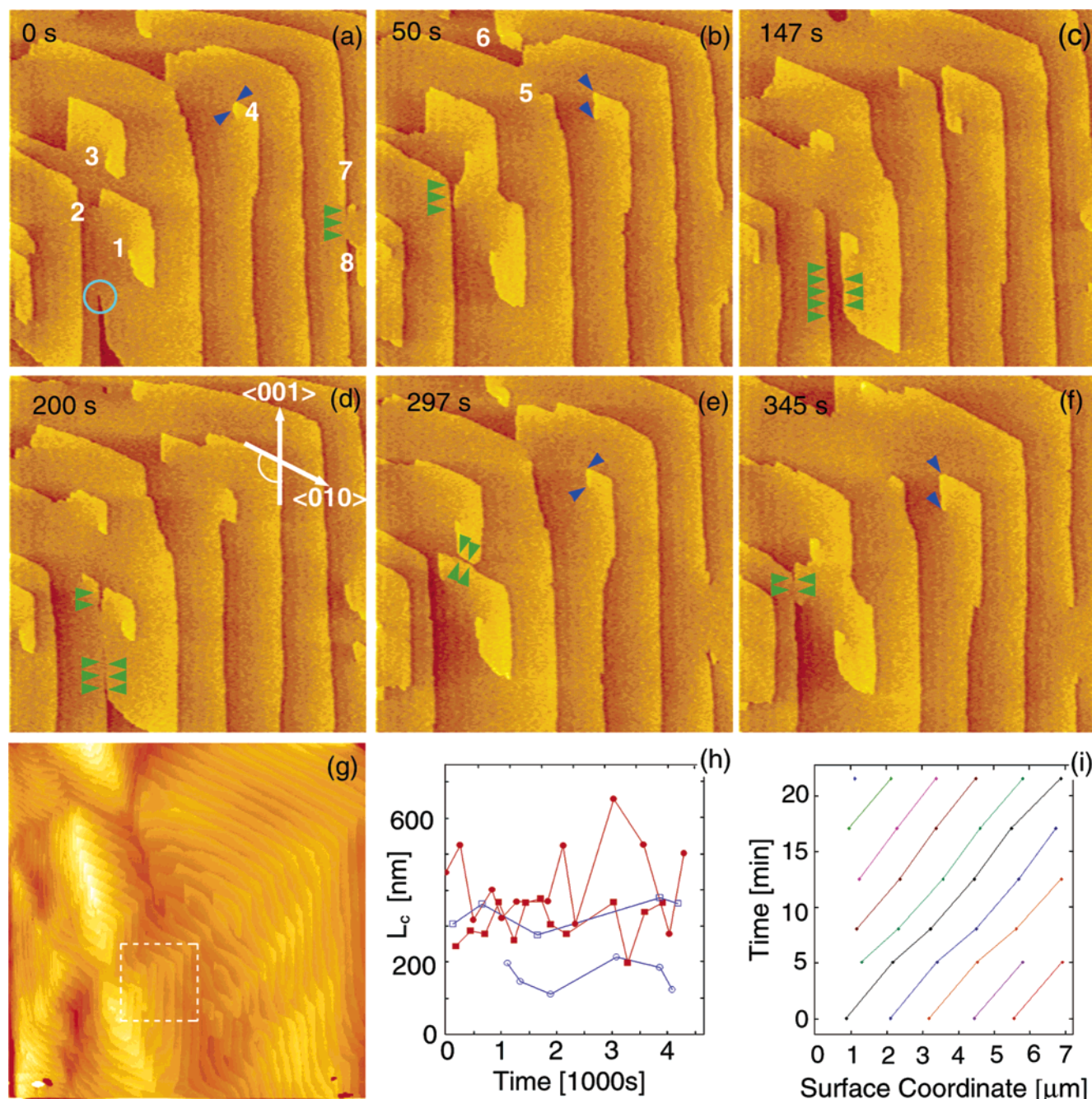(53) Wang, M.; X. B.Yin; Vekilov, P. G.; Peng, R. W.; Ming, N. B. *Phys. Rev. E* **1999**, *60*, 1901−1905.

Figure 6. Generation of steps at screw dislocations. (a)−(f) A time-lapse series of 9.5 × 9.5 μm^2 (Z-scale: 30 nm) images of a group of screw dislocations (numbered 1−8) recorded at $\sigma = 3$. Acquisition times, in seconds, are shown in each frame. Green arrowheads point to the regions where steps generated by different sources merge. Steps making up the incoming angles (encircled in turquoise in (a) and also visible between the steps indicated with the green arrowheads in (d), (e), and (f)) are observed to be straight (concave steps are expected for steps which are close enough for their diffusion fields to interact). The crystallographic axes spanning the (100) face are indicated in (d); the white arc indicates the angle between the steps generated by the dislocation. Critical lengths L_c are calculated from successive AFM images as the average of the step length just before (a) and (e) and just after (b) and (f); (blue arrowheads) a new step has appeared (the new steps in (b) and (h) are parallel to the [010] direction). (g) A 45 × 45 μm^2 (Z-scale: 75 nm) image of the area surrounding that shown in (a)−(f). The area imaged in those frames is indicated with the white rectangle. This image was taken immediately after the series of smaller image in (a)−(f). No effect of the tip can be discerned. (h) The critical length L_c plotted as a function of time of observation for sources 1 (circles) and 4 (squares), directions [001] (blue, open symbols) and [0$\bar{1}$0] (red, filled symbols). L_c's change with direction and with the source, and, for a given source and direction, fluctuate with time. No correlation exists between the L_c fluctuations of the different sources. Data from other sources and directions is omitted, but present essentially the same picture. (i) Trajectories of 10 steps followed on images such as those shown in (a)−(g). Each point on the plot represents the distance from the source of a given step at a given time. Fluctuations in step velocity and interstep distance are visible.

Equation 10 is applicable to systems with a different L_c for each vicinal and is based on the assumption that steps with $L > L_c$ grow at a rate υ_i independent of their length.

To better understand the anisotropy in L_c, we show in Table 2 that there are at least two distinct L_c's: in the [010] and [0$\bar{1}$0] directions the weighted average L_c ~360 nm, while in the [001]

and [00$\bar{1}$] directions, L_c's are shorter and the weighted average is ~240 nm. Equation 8 indicates that the anisotropy and asymmetry of L_c reflects the anisotropy of the line tension γ_l, which is different from the asymmetry of β illustrated by Figure 2. Since some models assume isotropic γ_l and symmetric L_c,[13,54,55] we searched for additional evidence for anisotropic

Table 2. Values of L_c and Step Widths for Various Sources and Crystallographic Directions. Values $\pm$ Std. Deviation [nm] (Number of Measurements)

source		direction			
		[010]	[001]	[0$\bar{1}$0]	[00$\bar{1}$]
1	L_c	368 $\pm$ 142 (13)	175 $\pm$ 45 (6)	453 $\pm$ 119 (13)	244 $\pm$ 71 (10)
	l	1062 $\pm$ 210 (8)			
3	L_c	343 $\pm$ 131 (10)		297 $\pm$ 12 (2)	267 $\pm$ 98 (9)
	l		$-$		
4	L_c		359 $\pm$ 47 (5)	331 $\pm$ 60 (13)	212 $\pm$ 57 (7)
	l	$-$	954 $\pm$ 103 (9)		

γ_l. In Figure 7 we show the hollow cores around the outcrop points of screw dislocations at conditions near the equilibrium between crystal and solution. While the size of the hollow cores varies, likely in response to surface supersaturation fluctuations, the shape is a parallelogram. Since at equilibrium this shape is solely determined by γ_l of the layers lining the core walls,[56] we conclude that the polygonal shape indicates anisotropy of γ_l.

Note that because of the depletion of the solution adjacent to the crystal surface and the related surface supersaturation decrease, evaluation of the line tension of the step γ_l from the two L_c values would be poorly justified.

To justify the assumption of the length-independent rate of step propagation for steps longer than L_c, we note that the rate of growth of short steps depends on their length L as[13]

$$v_i(L) = v_{i,\infty}\left\{1 - \frac{[\exp(\Delta\mu L_c/L\,kT) - 1]}{[\exp(\Delta\mu/kT) - 1]}\right\} \quad (11)$$

At $\Delta\mu/kT < 0.2$, this yields the commonly used[7]

$$v_i(L) = v_{i,\infty}(1 - L_c/L) \text{ or } v_i(\rho) = v_{i,\infty}(1 - \rho_c/\rho). \quad (12)$$

Direct calculations show that while with eq 12, $v_i(L) = 0.9v_{i,\infty}$ only at $L \sim 10L_c$, eq 11 indicates this occurs at $L \sim 2.5L_c$ for $\Delta\mu/k_BT = 1.4$, $\sigma = 3$, as in Figure 6. Thus, the use of eq 11 is justified for comparison with Figure 6, and its predictions are close to the assumption underlying eq 10.

Using the anisotropy ratios from eq 7 and $\alpha_i = \alpha = 114.8°$, with the above values of L_c, eq 10 yields $l_{\langle 001\rangle} = 1400$ nm and $l_{\langle 010\rangle} = 930$ nm, close to the actual observations in Table 2. This correspondence suggests that the main assumptions behind eq 10 are applicable to the generation and initial growth of layers during crystallization of insulin. Note that the kinetic coefficients enter eq 10. only as ratios accounting for the 2D anisotropy. Thus, we have shown that (i) the capillary lengths L_c are the only factors that determine the step density in the growth spiral, and (ii) since at $L > L_c$ $v_i(L) = v_{i,\infty}$, this is the only effect that capillarity has on the growth kinetics.

(54) Chernov, A. A.; Rashkovich, L. N.; Mkrtchan, A. A. *J. Cryst. Growth* **1986**, *74*, 101−112.
(55) Vekilov, P. G.; Kuznetsov, Y. G.; Chernov, A. A. *J. Cryst.Growth* **1992**, *121*, 643−655.
(56) Van den Hoek, B.; Van der Eerden, J. P.; Bennema, P. *J. Cryst. Growth* **1982**, *56*, 621−632.
(57) Malkin, A.; Kuznetsov, Y.; McPherson, A. *Surf. Sci.* **1997**, *393*, 95−107.
(58) Vekilov, P. G.; Ataka, M.; Katsura, T. *J. Cryst. Growth* **1993**, *130*, 317−320.
(59) Malkin, A. J.; Land, T. A.; Kuznetsov, Yu. G.; McPherson, A.; DeYoreo, J. J. *Phys. Rev. Lett.* **1995**, *75*, 2778−2781.
(60) Kuznetsov, Y. G.; Konnert, J.; Malkin, A. J.; McPherson, A. *Surf. Sci.* **1999**, *440*, 69−80.
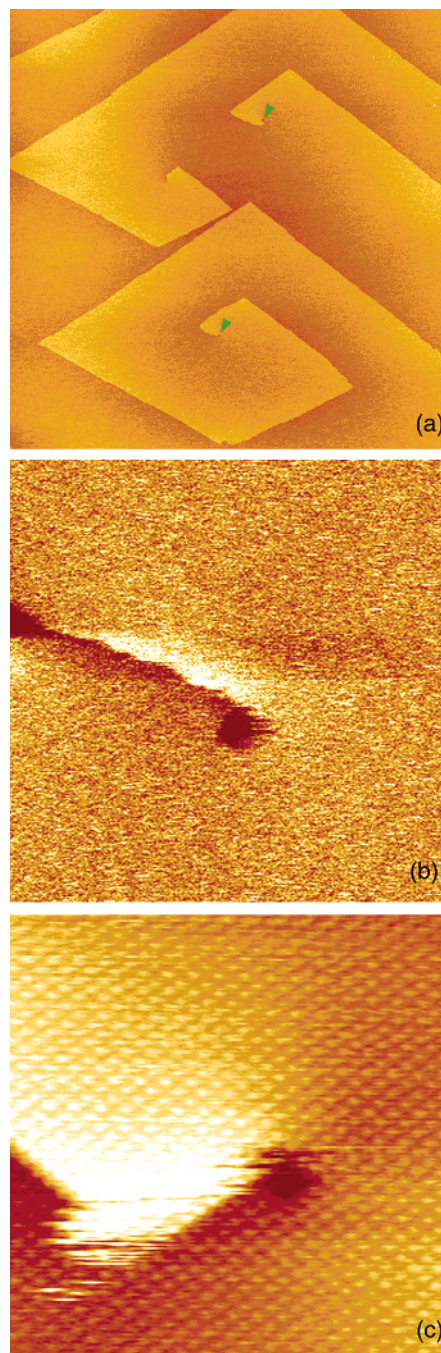

Figure 7. Dislocation hollow cores. (a) A tapping mode image of a group of dislocations at near-zero supersaturation. While the crystal is still growing, the dislocation cores (green arrowheads) are hollow. Image size: 5.8 μm. Z-scale 140 nm. (b) One of the dislocations shown in (a), imaged at a higher magnification. Note the noncircular shape of the hollow core. Image size: 600 nm. Z-scale 25 nm. (c) A contact mode, high-resolution image of another hollow core on the same crystal. The crystal lattice and the molecules at the edge of the growing step and at the core boundary are clearly resolved. The core is a parallelogram with sides of three and four molecules. The lattice distortion is due to the use of the O-ring during imaging. Image size: 200 nm. Z-scale: 8 nm.